Simultaneous seismic and magnetic measurements in the Low Noise Underground Laboratory (LSBB) of Rustrel, France, during the 2001, 26th january Indian earthquake

Stéphane Gaffet, Y. Guglielmi, J. Virieux, G. Waysand, A. Chwala, R. Stolz, Christophe Emblanch, M. Auguste, D. Boyer, A. Cavaillou

Geophys. J. Int. (2003) **155,** 981–990

Simultaneous seismic and magnetic measurements in the Low-Noise Underground Laboratory (LSBB) of Rustrel, France, during the 2001 January 26 Indian earthquake

S. Gaffet,[1] Y. Guglielmi,[2,1] J. Virieux,[1] G. Waysand,[3,4] A. Chwala,[5] R. Stolz,[5] C. Emblanch,[6] M. Auguste,[4] D. Boyer[4] and A. Cavaillou[4]

[1] *UMR Géosciences Azur,* 250, *rue Albert Einstein,* F-06560 *Sophia-Antipolis, France*
[2] *Université de Franche-Comté,* F-25030 *Besançon, France*
[3] *Groupe de Physique des Solides, Tour* 23, *Universités Paris VI, Marie Curie et Paris VII, Denis Diderot,* F-75251 *Paris Cedex* 05, *France*
[4] *LSBB, Université d'Avignon et des Pays de Vaucluse, La Grande Combe,* F-84400 *Rustrel, France*
[5] *IPHT Jena,* PF 100239, G-07702 *Jena, Germany*
[6] *Laboratoire d'Hydrogéologie, Université d'Avignon et des Pays de Vaucluse,* F-84000 *Avignon, France*

Accepted 2003 August 6. Received 2003 July 15; in original form 2002 June 6

SUMMARY

Since the decommission of the underground launching control room of the ground-based component of the French nuclear missile system, the whole installation has been turned into a cross-disciplinary underground laboratory. The LSBB is a unique low-noise underground laboratory because of its initial military conception and its location in the regional park of Luberon far from large cities, industry and heavy traffic. The deepest point is 500 m below the surface. At this depth a huge and non-conventional shielded cylindrical capsule is installed with no μ-metal, 1268 m^3 in volume, with a residual electromagnetic noise lower than 2 fT $Hz^{-1/2}$ above 10 Hz. As a result, fluctuations of the Earth's magnetic field under 10 Hz can be recorded at a very low-noise level with a low-T_c SQUID 3-D magnetometer. Taking advantage of the main gallery topology, a broad-band underground seismic array has been deployed since 2001. An analysis of data recorded simultaneously by the seismic underground array and by the magnetometer sensors during the Indian earthquake of 2001 January 26 is presented. Evidence of a magnetic field perturbation induced by the seismic waves at teleseismic distance (6250 km) is supported by a polarization analysis of seismic and magnetic signals. Spectral analysis shows specific frequency bands of perturbation related to physical processes such as ground water flow acceleration within the mountain structure.

Key words: electrokinetic coupling, electromagnetic shielding, hydromechanical simulation, LSBB, seismological array, seismomagnetic conversion, SQUID, underground laboratory.

1 INTRODUCTION

Many different observations of electromagnetic signals have been reported in relation to seismic phenomena occurring in the crust. Both electric and magnetic signals have been recorded under different environmental and experimental conditions (Fujinawa & Takahashi 1998; Perrier *et al.* 1998; Garambois & Dietrich 2001). As superficial seismic excitation of the subsurface may induce an electromagnetic signal, recent theoretical advances concerning the coupling between Maxwell's equations and the elastodynamic equations for a fluid-saturated porous medium (Pride 1994) provide a global framework for understanding the generation of such electromagnetic signals.

Two contributions to the electromagnetic field have been identified (Garambois & Dietrich 2001):

(1) electromagnetic perturbations induced by a fluid-pressure gradient in the volume that occur inside the seismic wave itself and

(2) electromagnetic disturbances that occur when seismic waves cross an interface with contrasting seismic or electric properties such as a water table at shallow depth.

Environmental noise such as the 50 Hz electric signal make the detection of electric signals related to seismic waves difficult. In addition, magnetic pollution from different human and natural sources may be expected and may dominate the magnetic signal related to seismic wave propagation.

In this paper, we present and analyse simultaneous observations of seismic and magnetic signals recorded under very carefully controlled experimental conditions at the Low-Noise Underground

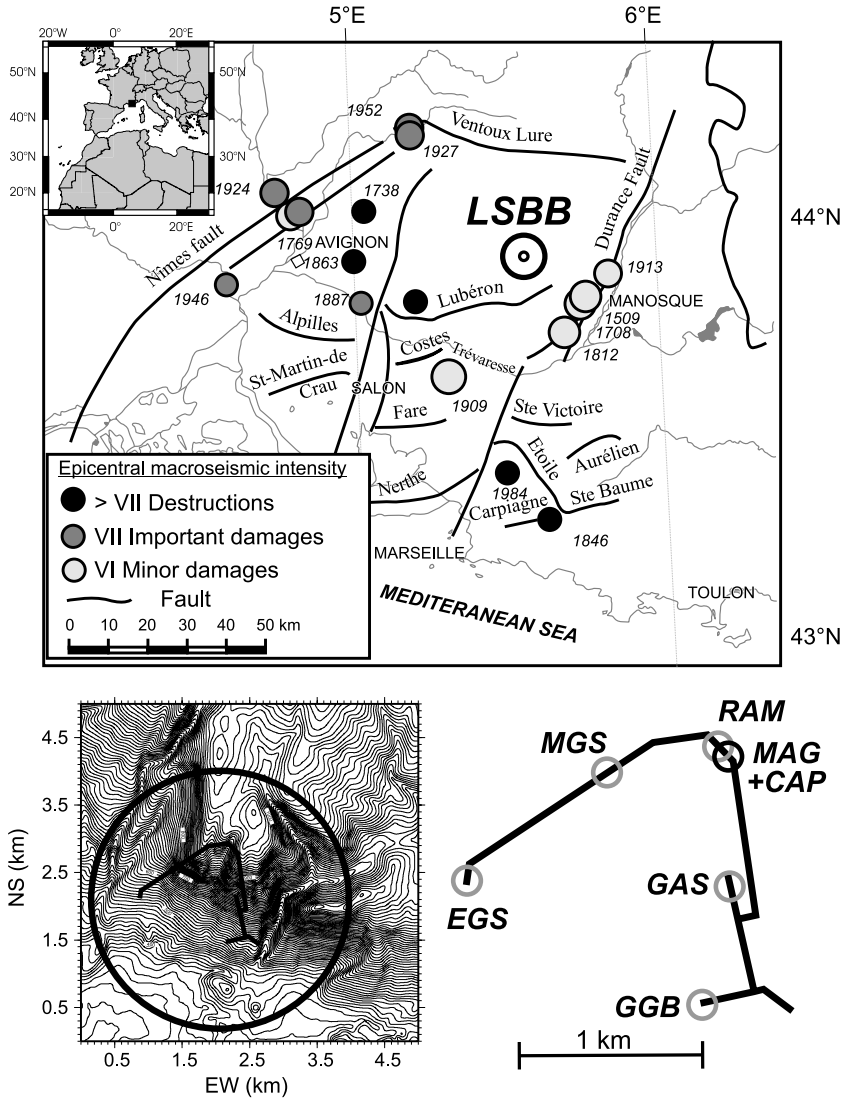

Figure 1. Location of the LSBB in the southeast part of France, modified from Lambert (1997) and geometry of the underground laboratory with instrumentation deployed in 2001 January. The grey circles indicate the STS2 seismic sensor locations of the underground array. The black circle locates the simultaneous magnetic and seismic sensors.

Laboratory (LSBB, Laboratoire Souterrain à Bas Bruit). By chance, an $M_w = 7.5$ earthquake occurred on 2001 January 26 in India while a preplanned experiment of simultaneous recording of seismic and magnetic signals was being undertaken for an estimation of the very low-noise and quiet magnetic environment. Previous comparisons have been performed for electromagnetic signals recorded in the vicinity of different hypocentres (Molchanov *et al.* 1992; Fujinawa & Takahashi 1998; Kawate *et al.* 1998; Telesca *et al.* 2001). We present here the very novel situation of the detection of magnetic signals at 6250 km away from the seismogenic region. At such a distance, no mechanical changes issuing from the epicentral area are expected and electromagnetic perturbations emitted from the seismogenic area can also be ruled out. Therefore, only a local origin, such as ground water acceleration, can be considered responsible for electromagnetic signals related to seismic wave propagation.

Some authors have speculated that mechanical and electromagnetic couplings take place in the earthquake zone that are generated by stress variations expected before, during and after an earthquake. The relation between electromagnetic and seismogenic evolution prior to an earthquake has long been a very controversial matter (Varotsos & Alexopoulos 1984; Varotsos *et al.* 1993; Molchanov *et al.* 1998; Pham *et al.* 2001) and systematic continuous observation should be performed before any assessment of such relation. The LSBB, located near two seismogenic fault systems (Fig. 1), might be a valuable place where such an investigation can be performed. Although these phenomena are related to the physical properties we analyse, we shall not investigate these aspects further in this paper.

Section 2 evaluates the low-noise environment of the LSBB as a result of the combination of natural conditions and the engineered shielding structure. In Section 3 we describe the experimental protocol used for the detection of the signals from the Indian earthquake, while in Section 4 we discuss possible interpretations.

2 LOW-NOISE UNDERGROUND LABORATORY (LSBB)

The LSBB is located in the southern 'Plateau d'Albion', north of Aix-en-Provence, France, under the 'Grande Montagne' massif. It

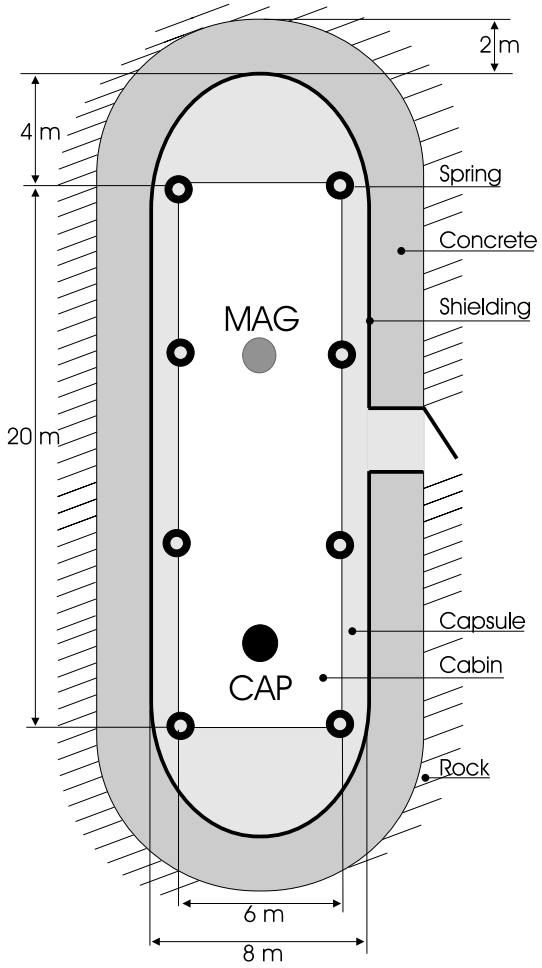

Figure 2. The 'Faraday cage' is a large cylindrical volume (capsule) shielded by a 1 cm thick stainless steel embedded in 2 m thick reinforced concrete. A cabin is suspended inside.

was the launch control centre for the French strategic nuclear defence (Fig. 1). This installation has been designed and built in order to remain operational even in the case of a nearby nuclear blast. As a result, it is resistant to radioactive clouds, thermal impacts, mechanical waves and electromagnetic pulses. Since 1997, it has been decommissioned for civil experimental research in a low-noise environment. It includes more than 3.5 km of galleries with horizontal access and an average slope of 2 per cent (Fig. 1). A large and unconventional Faraday cage is located at the deepest point, 500 m under the surface. The Faraday cage shape is a cylinder 28 m in length and 8 m in diameter (Fig. 2). Inside this cage, a cabin measuring 20×6 m^2 weighing 30 t is suspended using eight springs. These springs were designed to attenuate shock waves that would have been induced by the impact of direct explosions at the surface of the 'Grande Montagne' massif. The seismic and magnetic measurements that were performed in the capsule are described in the next paragraph.

2.1 Magnetic characteristic of the shielded capsule

The shielding effect within the capsule is the result of electromagnetic wave damping both by karstic 500 m thick rocks loaded with water, and by the 2 m thick reinforced concrete capsule with its 1 cm thick steel inner coating. The natural shielding provides a high-frequency cut-off around 200 Hz, whereas the concrete and steel wall reduce it to 10 Hz. In other words, this unusual combination is equivalent to a conventional Faraday cage but without μ-metal. Below 10 Hz, as for a conventional Faraday cage, there is no shielding (in the usual 'zero Gauss shielding' the damping of the low-frequency magnetic field is provided by current-controlled Helmholtz coils).

However, in the LSBB capsule, a DC magnetic field attenuation is noticed. We compare hereafter the amplitude of variation of the magnetic field with the amplitude of the quasi-static magnetic field. The signal of the magnetic field inside the capsule over 14 h of night time from 2001 January 25 to 26, has been processed. The recorded field is compared with the permanent geomagnetic signal of the Chambon-La-Forêt observatory (CLF). The modulus of the absolute magnetic field recorded at CLF is compared with the variation of the magnetic field modulus in the capsule (upper part of Fig. 3). CLF and LSBB fields are sampled at 1/60 and 125 Hz, respectively. Taking into account the short duration of the simultaneous recordings, the spectral comparison of field variation is shown for periods ranging from 120 to 10 000 s in the lower part of Fig. 3. The general trend of the magnetic field modulus is $1/f$ over this frequency range.

This result confirms the observations of Bloyet & Dolabdjian (1998) and Waysand *et al.* (2000). Between 2×10^{-4} Hz (i.e. 5000 s period) and 2×10^{-3} Hz (i.e. 500 s period), the magnetic field variation appears to be 1.5 larger than that observed at CLF. This observation cannot be fully explained without a simultaneously performed magnetic measurement outside the capsule. For frequencies between 3×10^{-3} Hz (i.e. 300 s period) and 10^{-2} Hz (i.e. 100 s period), the variation of the magnetic field recorded inside the capsule is half that of the CLF variation. Using the same set of data Zakosarenko *et al.* (2001) have shown that, for frequencies above 10 Hz, variations of the magnetic field are fully damped and remain lower than 2 fT Hz$^{-1/2}$, the intrinsic noise level of the SQUID magnetometer (van Duzer & Turner 1981).

The modulus of the quasi-static magnetic signal is reduced by a factor of 9 inside the capsule. Waysand *et al.* (2000) have shown that the magnetic field is approximately 5000 nT inside the capsule, compared with 47 000 nT measured at CLF. The quasi-static magnetic field amplitude variations are well correlated between the two sites.

3 SEISMOMETRIC AND MAGNETOMETRIC INSTRUMENTATION

Taking advantage of the topology of the galleries, an underground seismic array made up of five broad-band STS2 sensors (frequency band [0.02–120 s]) has been deployed (see the grey circles in Fig. 1). This seismic array allows a comparison between seismic signals recorded in the suspended cabin and seismic signals recorded in the tunnel. Azimuthal and apparent velocity characterization of the seismic wave front as well as the particle motions are determined using array analysis tools (Gaffet *et al.* 1998, 2002), which allow us to fully identify the induced excitation of the 'Grande Montagne'. The excitation is generated by the seismic vibrations issued from the Indian earthquake that occurred at $3^{\rm h}16^{\rm m}41^{\rm s}$TU, 2001 January 26. This event was located at 23.399°N, and 70.316°E, at 17 km depth with a magnitude $M_w = 7.5$. The backazimuth of the source is N89°.

Simultaneously with the array recording, the magnetic and the seismic fields were recorded inside the capsule within the

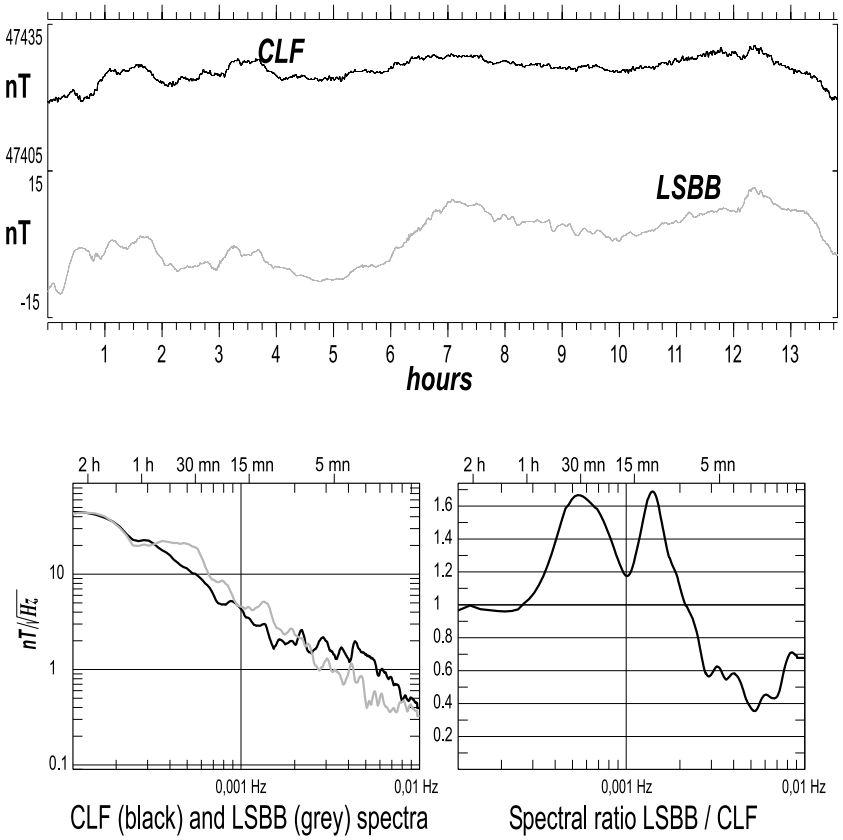

Figure 3. Comparison between the Chambon-la-Forêt (CLF) observations and the LSBB measurements of the magnetic field modulus over the 14 h time window of the experiment and spectral ratio associated.

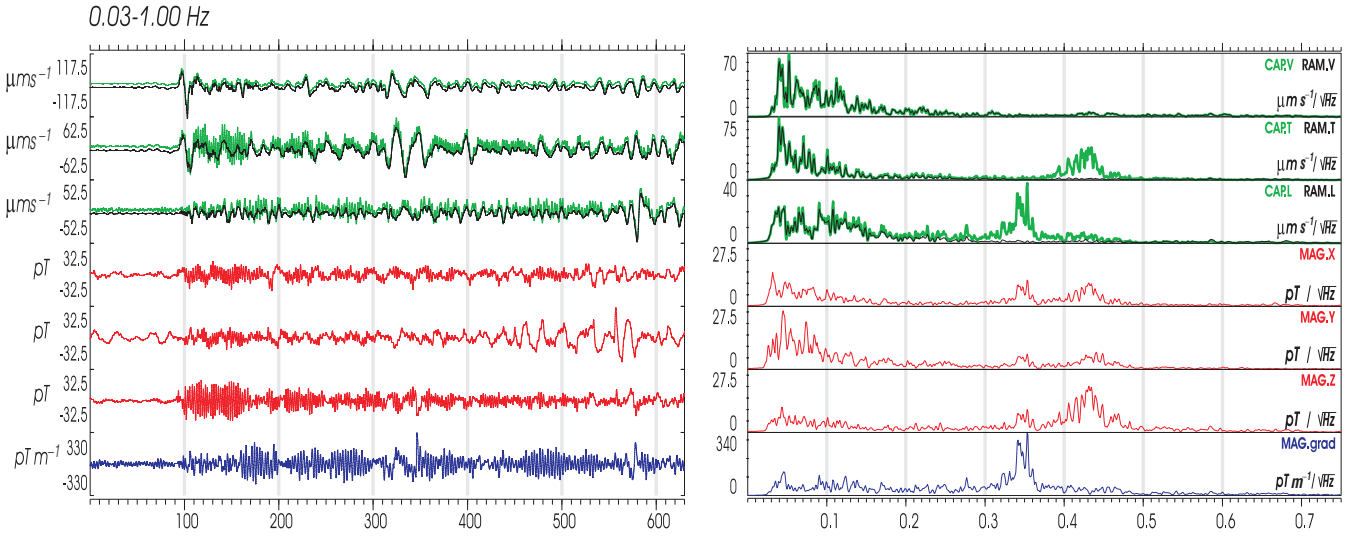

Figure 4. Seismic and magnetic raw signals: left, time variations; right, deduced spectra.

suspended cabin. The latter records were performed with a low critical temperature SQUID three-axis magnetometer and gradiometer (see http://www.ipht-jena.de/BEREICH_1/abt13_cryo_electronics for a description of the device), and with a STS2 seismic broadband sensor (see http://www.kinemetrics.com/products.html), respectively.

In Fig. 4, the V component of the seismometers corresponds to the vertical axis, the T component is horizontal and transverse to the capsule axis, and the L component is horizontal and longitudinal to the main capsule axis. In order to avoid confusion, the Y component for the magnetometer parallels the local north–south direction inside the shielding (turned clockwise by 60° from the longitudinal axis of the capsule), the X component is horizontal and perpendicular to the former, and the Z component is vertical. The component named grad is the vertical gradient of the X magnetic field component.

The seismic sensor labelled RAM is one of the five array sensors. It is located in a vault approximately 50 m north of the Faraday cage. The waveforms recorded by this sensor are used as the reference ground motion with no significant influence from the cabin oscillation. The seismic station within the cabin is called CAP and the SQUID magnetometer sensor, located 8 m from CAP, is labelled MAG.

4 DATA PRESENTATION AND ANALYSIS

The seismic waveforms of RAM (black line) and CAP (green line) are superimposed to compare the ground motions recorded in their respective environments (Fig. 4). This comparison allows a characterization of the mechanical transfer function of the suspended cabin. Both the seismic and the magnetic waveforms are filtered in the frequency bandwidth [0.03–1.00 Hz] that corresponds to the dominant frequency band of both the seismic ground excitation and characteristic mechanical resonances of the cabin.

A comparison between the spectra of the vertical components of CAP and RAM shows that no significant vertical vibration is induced by the cabin suspension during the Indian earthquake. Both waveforms and spectra for the vertical components are fully identical.

The cabin presents two wide ranges of horizontal resonant frequencies. The first broad resonance is in the [0.30–0.37 Hz] band: it is only recorded along the longitudinal cage axis (L component CAP.L). The second broad resonance covers the [0.37–0.47 Hz] range: it is only recorded by the T component CAP.T. These two resonance bands do not overlap each other and show equivalent rms spectral amplitudes (i.e. 40 μm s^{-1} Hz$^{-1/2}$). These horizontal mechanical vibrations are not transmitted significantly to the surrounding medium of the capsule, as shown by RAM records.

As a result, the spectrum is split into two bands. The first one is related to the seismic excitation identified by the bandwidth of the vertical component and covers the frequency range [0.03–0.25 Hz]. The second band is related to the mechanical behaviour of the suspended cabin and covers the frequency range [0.25–0.5 Hz]. These two frequency bands are within the linear response frequency band of both the seismometer (from 1/120 to 50 Hz) and the SQUID magnetometer (0–100 kHz). As a result the spectra are free of instrumental frequency limitations and can be directly discussed without pre-processing.

4.1 Magnetic field related to cabin resonances

In the frequency band corresponding to the cabin vibration [0.25–0.5 Hz] two resonance peaks are identified: [0.25–0.37 Hz] and [0.37–0.5 Hz]. The lowest resonance is a longitudinal mode (CAP.T is small), whereas the highest resonance is a transverse vibration mode of the cabin (CAP.L vanishes).

For each mode, all along the 600 s window, the seismic and magnetic signals have almost correlated instantaneous amplitudes as shown in Fig. 5 (top panel) where the corresponding moduli are superimposed in arbitrary linear vertical units.

At first glance, a magnetic coupling of the seismometer with the SQUID magnetometer could be suspected. This possibility is at odds with a crude study of the signal polarizations. Indeed, for each resonance the respective polarization spectra of the magnetic and of the seismic signals (right-hand part of Fig. 5) are clearly independent.

In the longitudinal mode, the magnetic field fluctuation peaks sharply towards the north magnetic pole within the cabin at 60°, whereas the polarization of the mechanical vibration of the suspended cabin fluctuates over half a circle. In contrast, in the transverse mode, since the epicentre of the event is in the transverse direction, the cabin vibrates in this azimuth, whereas the magnetic orientation fluctuation spreads over 90°. If a noticeable magnetic coupling between both devices had occurred, the seismic and the magnetic azimuthal spectra would have been correlated. In addition, both instruments having a wide band frequency response, the conclusion drawn from the cabin vibrations is also valid all over the seismic frequency band. Instrumental coupling may thus be ruled out.

4.2 Magnetic field related to seismic excitation

Wavenumber analysis shows that the azimuth distribution of arrivals is mainly centred around N100° ± 3° (Fig. 6). The successive body wave trains (*pP* mixed with *P*, *PcP*, *PP*, *PPP*, *PKiKP*, then followed by *S*, *PS* and *SP*) are mainly identified as plane waves. Thus the 'Grande Montagne' area, surrounding the array, appears to be subjected during the first 450 s, to compressive vibrations with successive incidence angles of 21° for *P*, 11° for *PcP*, 27° for *PP*, 30° for *PPP* and 4° for *PKiKP*. These are approximated as vertically incident plane waves for the hydromechanical simulation precessed in the next section.

In contrast with previous observations, the ground vibration is not at all linearly transferred to the magnetic field (Fig. 6). In this frequency band, which is far from its resonance modes, the cabin can be considered motionless with respect to the surrounding rock. Indeed, the vibrations recorded by CAP inside the capsule and RAM, 50 m outside, are identical just as if the RAM rock environment and the whole capsule were a single rigid body. Given that our interpretation of the preceding data is correct, then as a result, the observed magnetic variation can be ascribed to the motion of the 500 m thick Vaucluse aquifer that saturates the karst and fractured area up to 200 m below the LSBB.

4.3 Numerical simulation

The simultaneous recording of seismic and magnetic data show that induced magnetic fields are generated by at least two main physical processes: (1) a mechanical coupling induced by local vibrations of the suspended cabin inside the non-moving capsule and (2) the whole mountain and the surrounding region being shaken by a coherent source, considering that the analysed seismic wavelengths are in the range of 20–100 km. Pride (1994) proposed that electric currents may be generated by electrokinetic coupling induced by fluid acceleration. In the present case, is the regional seismic shaking able to produce such a fluid perturbation? This issue is discussed below. The possibility that magnetic fluctuations may have been induced by an electrokinetic coupling effect is investigated.

The fluid perturbation may have been activated at different scales, depending on the location of the fluid involved. Water is present in the karstic massif as ground water that occurs at different scales and different depths. It is mainly stored in the >10 km wide Vaucluse aquifer. This aquifer lies 200 m below the LSBB where it reaches 200–300 m in thickness. It thickens southward up to 1000 m (Fig. 7).

The fluid chemical composition is obtained from more than 196 samplings and described in Table 1 (Blavoux *et al.* 1992; Emblanch *et al.* 1998). This aquifer is mainly drained at the Fontaine de Vaucluse spring 30 km west of the LSBB, with a hydraulic

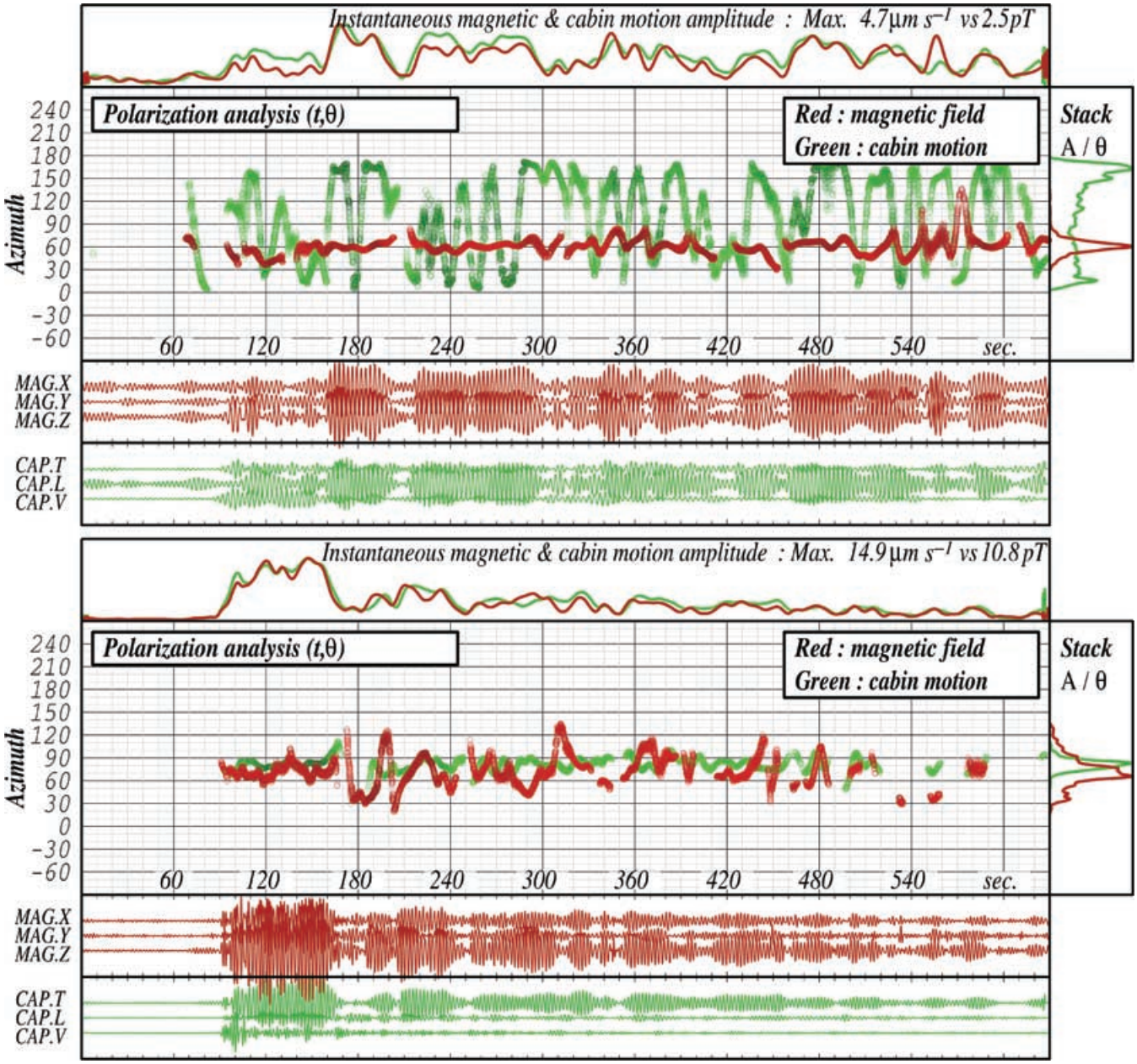

Figure 5. Polarization analysis of signals filtered in the longitudinal (upper panel) and transverse (lower panel) frequency bands of resonance.

gradient ranging between 0.14 and 1 per cent (Coutureaud 1993). It presents a conductivity of 425.5 μS with a mean temperature of 12.33°C.

The global electrical balance of the aquifer is nil. This zero charge is induced by the presence of clay with negative charges (Blavoux *et al.* 1992). The clay coats the inner side of the fluid-filled cavities and joints. The chemical characterization allows the aquifer to be considered a fluid electrolyte with an electrical charge greater than $\approx$450 C l^{-1}. Knowing that $\approx 150 \times 10^6$ m^3 of fluid are involved in the Vaucluse aquifer (Blavoux *et al.* 1992) and based on a mean karst porosity of 10^{-3} in volume, an electrokinetic phenomenon becomes possible. It could be caused either by aquifer flow acceleration or fluid particle acceleration. Both effects lead to motion of electrical charge, generating an electrical current which in turn could create the observed magnetic field perturbations.

The Vaucluse aquifer is a typical jointed karstified aquifer where groundwater can flow in two main types of joints more or less karstified.

(1) Faults and fractures of different extent (metres to kilometres) are distributed in two main families that trend N10°–60°E and N100°–140°E. Both dip steeply (80°–90°). At the aquifer scale (kilometres), spacing of macrofaults ranges between three and five faults km^{-2}. At the site scale, two main faults are displayed in the NS cross-section of the LSBB (Fig. 7).

(2) The sedimentary joints (bedding surface) attitude is N100°E/0°–20°S. The reservoir can be modelled as a stack of four main lithological units 100–500 m thick. Depending on the lithological units, stratification spacing ranges from a few centimetres to tens of meters.

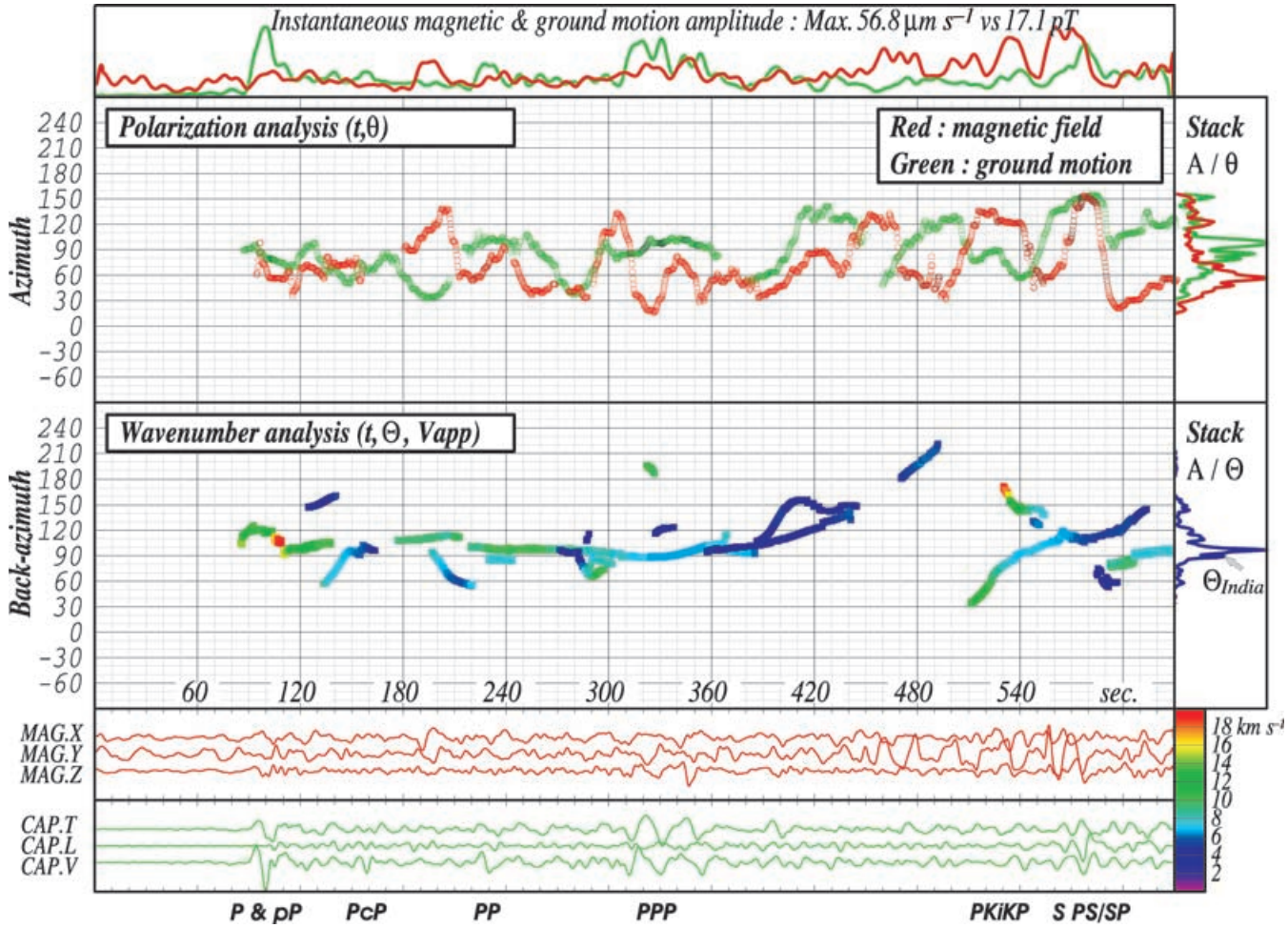

Figure 6. Polarization and wavenumber analysis with signal filtered in the seismic frequency band. Seismograms (green) and magnetograms (red) are presented in the bottom part. The second panel presents the apparent velocity versus time versus azimuth wavenumber analysis: the horizontal axis indicates the time, the vertical axis is the backazimuth of the wave arrivals. The coloured panel on the right indicates the apparent velocity convention. The right box contains the statistical distribution of energetic arrivals as a function of the azimuth. The polarization and the top panels are described in Fig. 5.

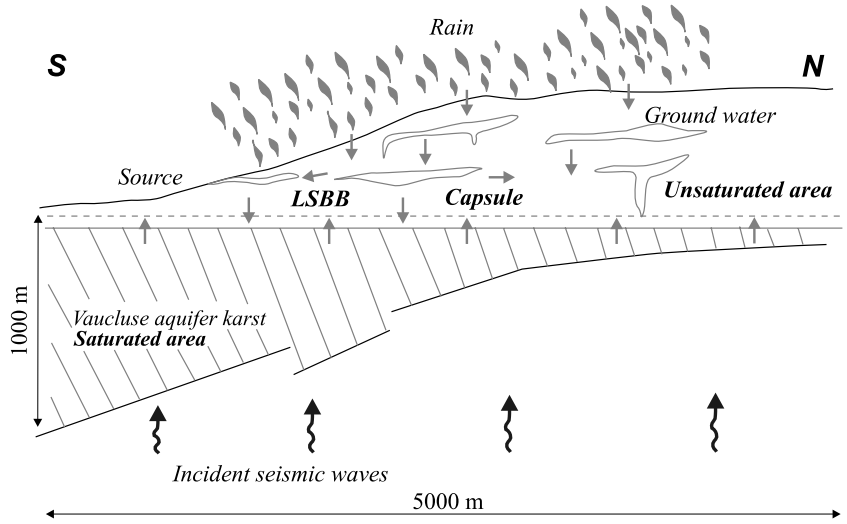

Figure 7. Geological NS cross-section of the LSBB: suspended aquifers are likely in the unsaturated area while the permanent aquifer lies 200 m below the LSBB tunnels.

Table 1. Chemical composition and electrical charge of the Vaucluse aquifer (Emblanch C. 2002, personal communication).

Ion	Charge	Density (mg l^{-1})	mol l^{-1}	Electrical charge (C l^{-1})
HCO_3	−	256.23	4.19930×10^{-3}	−405.177
SO_4	−−	12.69	0.13210×10^{-3}	−25.492
Cl	−	4.30	0.12129×10^{-3}	−11.703
NO_3	−	3.78	0.06096×10^{-3}	−5.882
Ca	++	84.36	2.10479×10^{-3}	+406.169
Mg	++	5.24	0.21553×10^{-3}	+41.592
Na	+	2.23	0.09700×10^{-3}	+9.359
K	+	0.50	0.01279×10^{-3}	+1.234

4.4 Aims of the UDEC modelling

The addressed question is the behaviour of the water inside the reservoir network stressed by the seismic wave excitation previously determined. The Universal Distinct Element Code (UDEC) (Cundall 1980) has the potential to model 1-D or 2-D (plane-strain or plane-stress) dynamic problems (Lemos 1987) in saturated or non-saturated rock masses. Different studies show that numerical results from UDEC calculations agree well with analytical solutions of wave transmission or reflection through a single fracture (Brady *et al.* 1998; Chen & Zhao 1998) and through a set of parallel fractures (Cai & Zhao 2000). UDEC calculations are also in good agreement with dynamic measurements (Bhasin *et al.* 1996) and physical models (Chryssanthakis *et al.* 1997) of underground openings. Dynamic computation in the UDEC code is based on an explicit time-marching scheme to solve the motion equation directly. This allows large finite displacements and deformations to be modelled, with the program being able to take into account new contact geometries that may appear during the deformation. In UDEC, deformation of fractured rock consists of elastic and/or plastic deformation of intact rock blocks, and of displacements along and across fractures (Pine & Cundall 1985). A fully coupled mechanical–hydraulical analysis is performed, in which the fracture conductivity is dependent on mechanical displacement of joint walls and on matrix deformation. Conversely, fluid pressure affects the mechanical behaviour (Last & Harper 1990). The fractured rock mass is modelled as a closely packed system of blocks with elastic properties. The blocks are impervious and bounded by fluid-filled fractures. At the contact between the blocks the fluid flow is calculated using the cubic power law (Witherspoon *et al.* 1980). The fracture aperture is approximated by a constant separation between two nodes of the block mesh and can be considered as two parallel plates. A minimum aperture value (residual aperture) is given hereafter in order to preserve the contact permeability. The larger the number of contacts is, the better the accuracy of the calculations.

4.5 Procedure of UDEC modelling

The UDEC procedure applies a dynamic loading to an initial calculation until it reaches a static equilibrium. The modelling consists of two successive stages. (1) The *y*-directed stress wave applied at the bottom of the model in order to calculate the amplitude of particle motion close to the LSBB capsule. (2) The water pressure and flow variation inside joints are determined at different locations in the reservoir submitted to this previously calculated dynamic loading.

The initial stress state is evaluated on the cross-section (Fig. 7), taking into consideration different scales, geometries and boundary conditions of models. A model cross-section of 1000 m long times 1000 m high with a planar topography is used (Fig. 8a). This extended geometry minimizes boundary effects in the LSBB zone. The joint network is made of two sets of horizontal and vertical fractures 1000 m long and spaced at 50 and 200 m, respectively, in order to represent the mean density and anisotropy of the site natural fracture network. Rock matrix and joint mechanical behaviour are assumed to be linearly elastic and isotropic. Rock and joint mechanical properties were taken from laboratory and *in situ* tests on similar limestones (Guglielmi & Mudry 2001). Young's modulus is $E = 50\,700$ MPa, the Poisson ratio is $\nu = 0.3$ and the density is 2000 kg m^{-3}. These values correspond to a *P*-wave velocity of 1936 m s^{-1} (C_P) and an *S*-wave velocity of 1449 m s^{-1} (C_S). In order to model the wave propagation accurately within the frequency band [0.05–0.15 Hz] a mesh size of $\lambda = 20$ m

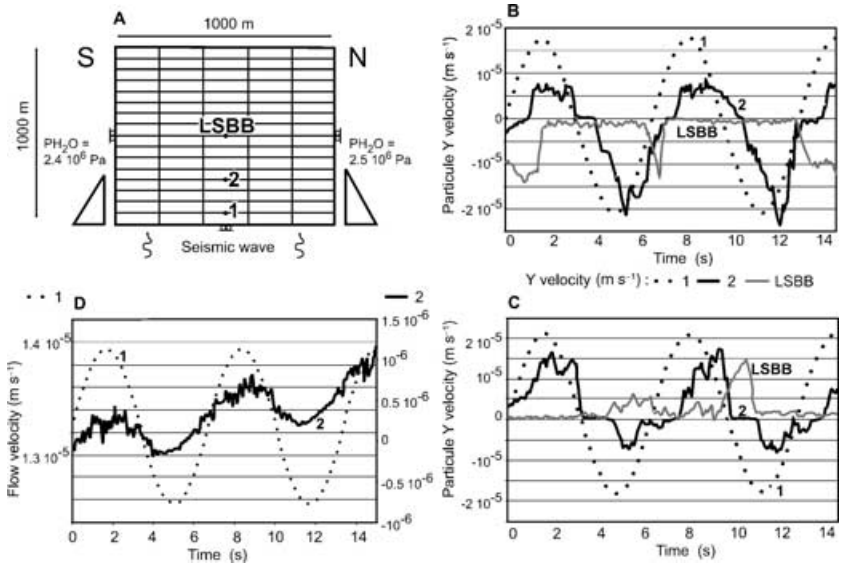

Figure 8. 2-D hydromechanical numerical model: (a) model geometry, location of calculation and boundary conditions. (b) Particle *y*-velocities at points 1, 2 and LSBB under dry conditions. (c) Particle *y*-velocities at points 1, 2 and LSBB with fractures filled with water at the basal part of the model. (d) Flow velocities at points 1 and 2 located inside two horizontal fractures.

is used in good accordance with a previously published guideline formula $f = C_S/10\ \lambda$ (Belytschko 1983). Joint mechanical characteristics are assumed to be constant along joints with values of normal stiffness $K_n = 1 \times 10^9$ Pa m^{-1} and shear stiffness $K_s = 0.1\ K_n$ Pa m^{-1}. The flow in the joints is set to be compressible. The water bulk modulus is $K_w = 20 \times 10^6$ Pa (this value equals 1 per cent of the real modulus, 2103×10^6 Pa, for pure water in order to take into account entrained air in groundwater). The same constant hydraulic aperture of 1×10^{-4} m is allocated to all the joints.

A hydraulic gradient of 0.01 is set from north to south. The hydraulic boundary conditions are 2.5×10^6 Pa on the north side and 2.4×10^6 Pa on the south side, the base of the model being impervious (Fig. 8a). A static hydromechanical calculation is performed with steady-state flow and fixed displacements at the bottom and lateral cross-section boundaries. Once static equilibrium is reached, various sinusoidal compressive *y*-directed stresses are applied at the bottom of the model until the calculated amplitudes of the particle *y*-velocity fit those measured at the LSBB capsule (Fig. 8a, point LSBB on the cross-section). No damping is applied to the model. Reflections at the boundaries are minimized using viscous boundaries at the bottom, the north and the south sides of the model. In order to test the effect of a basal saturated zone on wave attenuation, two tests with and without water were performed (in the latter case the flow was turned off and the water pressure was only taken into account in order to simplify the numerical calculations). A seismic wave frequency of 0.15 Hz is used for all tests. The last modelling stage consists of measuring pressure, flow velocities and particle *y*-velocities at two different points (1 and 2 in Fig. 8a), and particle *y*-velocities at the LSBB point (LSBB in Fig. 8a) under dynamic loading.

4.6 Modelling results

The particle motion required under the aquifer is found to be $\approx$105 μm s^{-1} in order to reach the typical particle velocity of 50 μm s^{-1} observed at the LSBB point. The calculated *y*-directed stress wave σ_n applied at the bottom of the model is $\sigma_n = 800 \sin(2\pi \times 0.15\ t)$. The presence of water filling the fractures is needed to preserve a coherent waveform at each test point (i.e. points corresponding to the seismic sensors of the underground array, Figs 8b and c). Without any water filling, particle *y*-velocity variations are very low at the LSBB point (Fig. 8b, curve LSBB). Diffusion predominates, generated by multiscattering of the incident wave by the fracture distribution. Wave transmission in a heterogeneous medium is a function of the ratio between fracture spacing and wavelength. It is also a function of the fracture shear stiffness (Cai & Zhao 2000). The simplified massif geometry modelled (Fig. 8a) only takes into account the much altered and penetrative fractures of the area. Experimental data on similar fractures imply one should use a low shear stiffness value that may explain the loss of coherence at the LSBB point (Fig. 8b). With a basal saturated 250 m thick zone, particle *y*-velocity variations at the LSBB point show a very different shape compared with the curves at points 1 and 2, which are both located in the water saturated zone (Fig. 8c curves 1, 2 and LSBB). The pressure variation ranges between 0 and 60 cm in water height. At points 1 and 2 (Fig. 8a) pressures variations values are 60 and 28 cm, respectively. Such variations correspond to water flow velocities in the ranging of 2–0.5 μm s^{-1} from the base to the upper level of the saturated zone. At the intermediate points 1 and 2 (Fig. 8d), located below the LSBB, the flow velocity variations are 1.2 and 0.5 μm s^{-1}, respectively.

Water pressure and flow velocity variations are explained by fracture volume deformation ΔV under drained conditions. A macrofracture can be considered a planar collection of connected collinear microvoids and asperities. The volumetric deformation of the voids and the deformation of the asperities explain the overall deformation of the fracture (Pyrak-Nolte 1988; Myer 1991). Such deformations induce water pressure variations in the case of fractures where ΔV and V (where V is the initial volume of the fracture void) are of the same order of magnitude. This means that the modelling results are only valid for low-conductivity fractures (fractures with low V values), according to the generally accepted cubic law. Such a dynamic loading does not cause any variation to large volumes such as karstic conduits and very permeable fractures. Actually the large very conductive volumes only represent 1–10 per cent of a reservoir fracture network (1 per cent in the case of the Stripa site, Olsson *et al.* 1989; Black *et al.* 1991) so that such an effect would have been negligible. Accordingly Guglielmi & Mudry (2001) established that water is mainly stored in the remaining 90–99 per cent of the small low conductive volumes.

5 CONCLUSION

We report the first observation of simultaneously recorded seismic and seismomagnetic signals at a 6250 km distance from the epicentre, of the 2001 January 26 Indian earthquake. This was performed using a high-quality underground seismic array combined with an ultrasensitive triaxial superconducting magnetometer (SQUID) operated at liquid helium temperature.

These devices could be operated at their maximum sensitivity due to the underground unusually low-noise environment of the Laboratoire Souterrain à Bas Bruit de Rustrel (LSBB in Vaucluse, France). The recorded signals, which have amplitudes three orders of magnitude below the usual level of measurements, show the ability of the LSBB to detect very low-amplitude signals. The absence of noticeable human activity all over the site is responsible for the quality of the seismic information, while a very special shielded room with no μ-metal provides residual magnetic noise lower than 2fT Hz$^{-1/2}$ above 10 Hz.

Our interpretation of these magnetic and seismic data, coupled with our understanding of theoretical results, led us to believe that the main source of the magnetoseismic signals recorded at the LSBB is the oscillation of the aquifer, itself caused by the passage of the seismic waves from a large earthquake at teleseismic range. The combination of transient acceleration of the aquifer flow on one hand and the fluid electrolyte particle acceleration on the other hand are responsible for the magnetic perturbations recorded.

We do recognize, however, that further analysis of both these and future data collected at LSBB may argue for alternative physical explanations. Installation of a permanent facility at LSBB to study these phenomena is now under consideration.

ACKNOWLEDGMENTS

This work was performed through funding of the 'Région Provence Alpes Côte d'Azur' (PACA), the 'Département du Vaucluse', the 'Communauté des Communes de Rustrel—Pays d'Apt', the 'Plan Pluri-Formation' LSBB from the 'Ministère de l'Éducation Nationale', the 'Commissariat à l'énergie Atomique, Département d'Analyse et de Surveillance de l'Environnement' (CEA/DASE), the 'Programme National des Risques Naturels' 2001 (PNRN), and the 'Fond de Restructuration des Établissements de Défense'

(FRED) in France. Seismic data were recorded using the 'Réseau Large Bande Mobile' (RLBM) of the 'Institut National des Sciences de l'Univers' (INSU). Magnetic data from CLF were recovered from the 'International Real-time Magnetic Observatory Network' (INTERMAGNET). We thank Tony Monfret and Jean Delteil from 'UMR Géosciences Azur' for fruitful discussions during the redaction of the manuscript. This paper is contribution no 511 of UMR Geosciences Azur.

REFERENCES

Belytschko, T., 1983. An overview of semidiscretization and time integration procedures, *Computational Methods for Transient Analysis,* Ch. 1, pp. 1–65, Elsevier, New York.

Bhasin, R.K., Barton, N., Grimstad, E., Chryssanthakis, P. & Shende, F.P., 1996. Comparison of predicted and measured performance of a large cavern in the Himalayas, *Int. J. Rock Mech. Min. Sci.,* **33,** 607–626.

Black, J., Olsson, J., Gale, J. & Holmes, D., 1991. Site characterization and validation—stage 4—Preliminary assesment and detail prediction, *Stripa Project TR91–08,* Stockholm, Sweden.

Blavoux, B., Mudry, J. & Puig, J.M., 1992. The karst system of the Fontaine de Vaucluse (Southeastern France), *Environmental Geol. Water Sci.,* **19,** 215–225.

Bloyet, D. & Dolabdjian, C., 1998. Champ statique et fluctuations dans la capsule du LSBB/Rustrel—12, 13 novembre 1998, *Rapport interne du GREYC à Caen,* France.

Brady, B.H., Hsiung, S.H., Chowdhury, A.H. & Philip, J., 1990. Verification studies on the UDEC computational model of jointed rock, in *Mechanics of Jointed and Faulted Rock,* pp. 551–558, ed. Rossmanith, H.P., A. A. Balkema, Rotterdam.

Cai, J.G. & Zhao, J., 2000. Effects of multiple parallel fractures on apparent attenuation of stress waves in rock mass, *Int. J. Rock Mech. Mining Sci.,* **37,** 661–682.

Chen, S.G. & Zhao, J., 1998. A study of UDEC modelling for blast wave propagation in jointed rock masses, *Int. J. Rock Mech. Mining Sci.,* **35,** 93–101.

Chryssanthakis, P., Barton, N. & Monsen, K., 1997. Dynamic loading of physical and numerical models of very large underground openings, *Proc. 8th Int. Congress on Rock Mechanics (Tokyo, September 1995)*, pp. 1313–1316, A. A. Balkema, Rotterdam.

Coutureaud, A., 1993. Hydrogéologie de la partie occidentale du système karstique de Vaucluse, *Thèse de troisième cycle,* p. 159, Université d'Avignon et des Pays de Vaucluse.

Cundall, P.A., 1980. A generalized distinct element program for modelling jointed rock, *Report* PCAR-1-80, Peter Cundall Associates, US Army, European Research Office, London.

Emblanch, C., Puig, J.M., Zuppi, G.M., Mudry, J. & Blavoux, B., 1998. Comportement particulier lors des montées de crues dans les aquifères karstiques, mise en évidence d'une double fracturation et/ou de circulation profonde: exemple de la Fontaine de Vaucluse, *Eclogægeol. Helv.,* **92,** 251–257.

Fujinawa, Y. & Takahashi, K., 1998. Electromagnetic radiations associated with major earthquakes, *Phys. Earth planet. Inter.,* **105,** 249–259.

Gaffet, S., Larroque, C. & Deschamps, A., 1998. Dense array experiment for observation of waveform perturbations, *Soil Dyn. Earth. Eng.,* **17,** 475–484.

Gaffet, S., Schisselé, E. & Plaut, G., 2002. Apport des antennes sismologiques pour l'analyse de l'influence régionale des hétérogénéités géologiques sur la propagation des ondes—les expériences de Caille 1994, Annot 1998 et du LSBB, 2001, *Cahier technique AFPS-CFGI 'Géologie et risque sismique',* pp. 49–57.

Garambois, S. & Dietrich, M., 2001. Seismoelectric wave conversions in porous media: field measurements and transfer function analysis, *Geophysics,* **66,** 1417–1430.

Guglielmi, Y. & Mudry, J., 2001. Quantitative measurement of channel-block hydraulic interactions by experimental saturation of a large, natural, fissured rock mass, *Groundwater,* **39,** 696–701.

Kawate, R., Molchanov, O.A. & Hayakawa, M., 1998. Ultra-low-frequency magnetic fields during the Guam earthquake of 8 August 1993 and their interpretation, *Phys. Earth planet. Inter.,* **105,** 229–238.

Lambert, J., 1997. *Les Tremblements de Terre en France,* p. 196, BRGM, Orléans.

Last, N.C. & Harper, T.R., 1990. Response of fractured rock subject to fluid injection. Part I: Development of a numerical model, *Tectonophysics,* **172,** 1–31.

Lemos, J.V., 1987. A distinct element model for dynamic analysis of jointed rock with application to dam foundation and fault motion, *PhD thesis,* p. 245, University of Minnesota, Minneapolis.

Molchanov, O.A., Kopytenko, Y.A., Voronov, P.M., Kopytenko, E.A., Matiashvili, T.G., Fraser-Smith, A.C. & Bernardi, A., 1992. Results of ULF magnetic field measurements near the epicenters of the Spitak ($M_S = 6.9$) and Loma Prieta ($M_S = 7.1$) earthquakes: comparative analysis, *Geophys. Res. Lett.,* **19,** 1495–1498.

Molchanov, O.A., Hayakawa, M., Oudoh, T. & Kawai, E., 1998. Precursory effects in the subionospheric VLF signals for the Kobe earthquake, *Phys. Earth planet. Inter.,* **105,** 239–248.

Myer, L.R., 1991. Hydromechanical and seismic properties of fractures, *Proc. 7th Int. Congress on Rock Mechanics,* **1,** 397–404.

Olsson, O., Black, J., Gale, J. & Holmes, D., 1989. Site characterization and validation stage 2—Preliminary predictions, *Stripa Project TR89–03,* Stockholm, Sweden.

Perrier, F., Trique, M., Lorne, B., Avouac, J.-P., Hautot, S. & Tarits, P., 1998. Electric potential variations associated with yearly lake level variations, *Geophys. Res. Lett.,* **25,** 1955–1958.

Pine, R.J. & Cundall, P.A., 1985. Applications of the fluid rock interaction program (FRIP) to the modelling of hot dry rock geothermal energy systems, *Proc. Int. Symp. on Fundamentals of Rock Joints,*, September 1985, pp. 293–302, Bjorkuden, Lapland, Sweden.

Pham, V.N., Boyer, D., Perrier, F. & Le Mouël, J.-L., 2001. Generation mechanisms of telluric noises in ULF band: possible sources for the so-called 'seismic electric signals' (SES), *C. R. Acad. Sci.,* **33,** 255–262.

Pride, S., 1994. Governing equations for the coupled electro-magnetics and acoustics of porous media, *Phys. Rev. B,* **50,** 15 678–15 696.

Pyrak-Nolte, L.J., 1988. Seismic visibility of fractures, *PhD thesis*, p. 234, Department of Materials Science and Mineral Engineering, University of California, Berkeley.

Telesca, L., Cuomo, V. & Lapenna, V., 2001. A new approach to investigate the correlation between geoelectrical time fluctuations and earthquakes in a seismic area of southern Italy, *Geophys. Res. Lett.,* **28,** 4375–4378.

van Duzer, T. & Turner, C.W., 1981. *Principles of Superconductive Devices and Circuits,* pp. 216–227, Elsevier, Amsterdam.

Varotsos, P. & Alexopoulos, K., 1984. Physical properties of the variations of the electric field of the earth preceding earthquakes, *Tectonophysics,* **110,** 73–98.

Varotsos, P., Alexopoulos, K. & Lazaridou, M., 1993. Latest aspects of earthquake prediction in greece based on seismic electric signals, *Tectonophysics,* **224,** 1–37.

Waysand, G., Bloyet, D., Bongiraud, J.P., Collar, J.L., Dolabdjian, C. & Le Thiec, Ph., 2000. First characterization of the ultra shielded chamber in the low noise underground laboratory (LSBB) of Rustrel-Pays d'Apt, *Workshop on Low Temperaure Devices (LDT8), August 1999—'Nuclear Instrumentation and Methods in Physics Research',* **A444,** 336–339.

Witherspoon, P.A., Wang, J.S.Y, Iawi, K., Gale, J.E., 1980. Validity of cubic law for fluid flow in a deformable rock fracture, *Water Res. Res.,* **16,** 1016–1024.

Zakosarenko, V., Stolz, R., Fritzsch, N., Oukhanski, N., Chwala, A., Schulz, M. & Meyer, H., 2001. LTS gradiometer/Magnetometer-SQUID system for magnetic field measurements, *Conference EUCAS 2001,* August 26–30, 2001, Copenhagen.